Engineering 17 (2022) 110–122

Contents lists available at ScienceDirect

Engineering

journal homepage: www.elsevier.com/locate/eng

Research
Civil Engineering Materials—Article

Three-Dimensional Mesoscopic Investigation on the Impact of Specimen Geometry and Bearing Strip Size on the Splitting-Tensile Properties of Coral Aggregate Concrete

Zhangyu Wu [a], Jinhua Zhang [b,c,*], Hongfa Yu [a,*], Qin Fang [d], Haiyan Ma [a], Li Chen [b,c]

[a] Department of Civil and Airport Engineering, Civil Aviation College, Nanjing University of Aeronautics and Astronautics, Nanjing 210016, China
[b] School of Civil Engineering, Southeast University, Nanjing 210096, China
[c] Engineering Research Center of Safety and Protection of Explosion and Impact of Ministry of Education (ERCSPEIME), Southeast University, Nanjing 211189, China
[d] Army Engineering University of PLA, Nanjing 210007, China

ARTICLE INFO

Article history:
Received 17 June 2020
Revised 19 January 2021
Accepted 2 February 2021
Available online 14 December 2021

Keywords:
Coral aggregate concrete
3D mesoscopic modelling
Splitting-tensile test
Tensile strength
Specimen geometry
Bearing strip

ABSTRACT

The use of coral aggregate concrete (CAC) as a novel construction material has attracted significant attention for the construction of reef engineering structures. To investigate the static splitting-tensile behaviors of CAC under the influence of two factors, namely specimen geometry and bearing strip size, a three-dimensional (3D) mesoscale modeling approach with consideration for aggregate randomness in shape and distribution was adopted in this study. We established 12 different specimen models with two specimen shapes (i.e., a cube with an edge length of 150 mm and a cylinder with dimensions of ϕ 150 mm × 300 mm) and six strip widths (i.e., 6, 9, 12, 15, 18, and 20 mm) for calculation. The effects of specimen geometry and strip width on the splitting-tensile properties of CAC, such as failure processes, final failure patterns, and splitting-tensile strength (f_{st}), are analyzed and discussed systematically. The results indicate the high reliability of the developed mesoscale modeling approach and reveal the optimal computational parameters for simulating and predicting the splitting-tensile properties of CAC. The f_{st} values of CAC are associated with both the specimen geometry and width of the bearing strip. The f_{st} values of the cube model are slightly higher than those of the cylinder model for the same bearing strip size, representing geometry effects that can be explained by differences in fracture area. Additionally, the f_{st} value of CAC gradually increases with the relative width of the bearing strip ranging from 0.04 to 0.13. Based on the elastic solution theory, the variation area of CAC f_{st} values with the relative width of the bearing strip was determined preliminarily, which has great significance for studying the tensile performance of CAC.

1. Introduction

It is well known that concrete is a quasi-brittle material, the tensile strength of which is much smaller than its compressive strength, implying that tensile damage to concrete is the main factor causing the destruction of concrete structures. Based on extensive theoretical analysis, experimental work, and numerical simulation [1,2], the splitting-tensile test is regarded as the most efficient method for the determination of concrete tensile strength, generally outperforming the direct tension test and modulus of rupture test. Generally, in a splitting-tensile test, the horizontal tensile stress in a concrete sample can be indirectly derived from an applied load along the vertical direction that divides the test specimen into half along the loading plane. Many researchers [3,4] have demonstrated that in the typical failure pattern of concrete specimens under split tension, many cracks occur along the loading direction and some compressive failure also occurs at the upper and lower loading positions. Therefore, the compressive stress concentrations that appear at the compressive loading positions lead to the dispersion of splitting-tensile strength, which is typically 5% to 10% greater than direct tensile strength [5]. The first splitting-tensile test for concrete was conducted by Carneiro and Barcellos [6] using a cylindrical specimen. This type of test has been acknowledged by the scientific community and is suggested in many standards, such as ASTM C496-90 [7], BS 1881-117 [8], ISO 4108 [9], and GB/T 50081 [10], for measuring concrete tensile strength.

* Corresponding authors.
E-mail addresses: zjh982038@163.com (J. Zhang), yuhongfa@nuaa.edu.cn (H. Yu).

https://doi.org/10.1016/j.eng.2021.02.024

Various specimen shapes, including cubes [11] and diagonal cubes [12], have also been employed to determine the tensile properties of concrete. The effect of specimen shape on concrete tensile strength was analyzed by Rocco et al. [13] based on linear elasticity theory, where the effects of local stress concentrations at loading points were considered. They concluded that the splitting-tensile strength of a cube specimen with an edge length of D is greater than that of a $D \times H$ cylindrical specimen (diameter $\times$ height) for a constant width of the bearing strip. A similar shape effect was validated through split-tension tests using large quantities of cubic (side lengths of 150 to 750 mm) and cylinder specimens (D values of 150 to 750 mm and D/H ratios of 1/2) by Zhou et al. [14]. Additionally, based on splitting tests and theoretical analysis using elasticity theory [1,15,16], it has been demonstrated that the splitting-tensile strength of concrete also depends on the width of the bearing strips placed between a concrete specimen and the corresponding loading points. Rocco et al. [17,18] found that the standardized formulas for calculating splitting strength are not applicable to concrete and are mainly affected by specimen geometry and strip width. Additionally, based on corresponding test results, Rocco et al. [19] demonstrated that the tensile strength in splitting-tensile tests without bearing strips is approximately 8% lower than that in the tests performed with bearing strips. Furthermore, according to available test and numerical results, tensile strength gradually decreases with the decrease of bearing strips width, and the influence of strip size on tensile strength can be ignored when the relative width of the bearing strip (b/D) is less than 4% [19]. However, there are no uniform criteria for the widths of bearing strips in split-cylinder/cube tests. For instance, the strip widths for static split-cylinder tests are recommended to be 25 mm and (15 ± 2) mm in the ASTM C496-90 [7] and BS 1881-117 [8] standards, respectively. The recommended strip widths for split-cube tests are 4 to 15 mm and 20 mm in the BS 1881-117 [8] and GB/T 50081 [10] standards, respectively. Therefore, it is still of great significance to analyze the effects of specimen geometry and bearing strip width on the static split-tension strength of concrete.

Based on the urgent need for engineering construction on islands and reefs worldwide, a novel type of lightweight concrete called coral aggregate concrete (CAC), which consists of coral aggregate, cement, seawater, and other admixtures, has attracted significant attention for its superior properties and the abundance of local resources, namely coral debris and seawater from reefs and islands [20,21]. During World War II, the US Naval Civil Engineering Laboratory conducted a series of experimental studies on the mixture proportions and basic mechanical properties (e.g., compressive strength, elasticity modulus, and flexural strength) of CAC comprising seawater and coral aggregates produced by various islands in the Pacific Ocean [22–24]. Subsequently, Scholer [25] and Howdyshell [26] examined and investigated the durability and strength of CAC structures in the Pacific islands. Chloride corrosion induced by coral aggregates and seawater was recognized as the primary threat to the durability of CAC structures and concrete strength was associated with the chloride content in the CAC. Based on the preparation principles of high-performance concrete and the "rich slurry theory" proposed by Yu et al. [27], high-performance CAC with compressive strength in the range of 30–70 MPa has been prepared and the corresponding mechanical properties have been investigated over the past few years [28]. Mi et al. [29] compared the splitting-tensile strength of CAC to that of ordinary Portland concrete (OPC) in the same strength grade (30–60 MPa), and found that the tensile strength of CAC is 9% to 33% greater than that of OPC. This strength difference decreases with an increasing strength grade. Ma et al. [30] investigated the static splitting-tensile strength of a CAC cylinder (ϕ70 mm $\times$ 70 mm) and compared their results to those presented by Mi et al. [29], who measured cube specimens with side lengths of 100 mm. They discovered that the tensile strength of the cylinder CAC specimen was significantly higher than that of the cube specimen. Therefore, specimen geometry does affect the splitting-tensile strength of CAC and must be investigated. Additionally, no literature exists on the effects of bearing strip size on the split-tension test results of CAC, which are of great importance for evaluating the practical tensile strength of CAC.

To capture the macroscopic properties and failure mechanisms of concrete under tension, mesoscopic approaches that assume concrete to be a two-, three-, or four-phase composite have been employed extensively to investigate the tensile behaviors of concrete [31–33]. Suchorzewski et al. [31] performed two-dimensional (2D) calculations using a discrete element model (DEM) to simulate the quasi-static splitting-tensile behaviors of concrete. Concrete was modeled based on micro-computed tomography (micro-CT) images of concrete mesostructures, where the macroscale voids in the concrete were considered. Similarly, based on 2D/3D X-ray micro-CT images, two types of mesoscale methods (finite element model (FEM) and DEM) were employed by Skarżyński et al. [32] to investigate the tensile behavior of concrete. The fracture behavior of concrete and the effects of the interfacial transition zone (ITZ) were studied numerically. Zhou and Hao [33] numerically investigated the dynamic tensile behavior of concrete at high strain rates using a 2D mesoscale model, in which aggregates were assumed to be circular and the ITZ was modeled as a thin boundary layer around the aggregates. Jin et al. [3] developed a 3D mesoscale model to investigate dynamic size effects on the splitting-tensile strength of concrete cube specimens. Failure patterns and processes in cube specimens under splitting tension were also simulated. They proposed a dynamic size effect law for the splitting-tensile strength of concrete. However, the aggregate model shapes in previously published mesoscale models are mainly circles (2D), polyhedrons (2D), and spheres (3D), which have limitations in terms of the representation of the randomness of aggregate shapes and distributions. Therefore, a 3D mesoscale model that considers the random shapes and distributions of aggregates in concrete should be developed and employed for concrete simulations.

The goal of this study was to investigate the effects of specimen geometry and the width of bearing strips on the splitting-tensile strength of CAC via numerical analysis employing a 3D random mesoscale modeling approach, in which CAC is assumed to be a tri-phase composite consisting of coral aggregate and mortar with an ITZ between these two phases. The coral aggregate is represented by the proposed 3D particle models with random shapes that are dispersed with random spatial locations and orientations within the mortar. CAC splitting specimens, including cubes with side lengths of 150 mm and cylinders with a diameter of 150 mm and height of 300 mm, were generated and static splitting-tensile simulations were performed using the commercial software ANSYS/LS-DYNA. Mesoscopic results for the CAC specimens under split tension, including failure processes, final failure patterns, and stress–displacement relationships, were obtained using a 3D mesoscale modeling method and compared with the observed test results. The effects of specimen geometry and strip width on the properties of CAC are analyzed and discussed. The corresponding shape effect and size effect laws for CAC tensile strength are analyzed through comparisons of numerical values and available test results to derive insights into the varying trends of CAC tensile strength and provide suggestions for splitting-tensile testing.

2. Mesoscale modeling approach

2.1. Random aggregate models

Compared to other mesoscopic models such as lattice models [34] and random particle models [35], random aggregate models

[36,37] that consider the random shapes of aggregates in concrete have been widely acknowledged and applied to investigate the mesoscopic properties of concrete. Additionally, the existence of an ITZ bonding between the aggregate and mortar matrix can be represented using limited-scale solid elements around random aggregate models [38]. Wittmann et al. [39] first employed 2D random circular models to simulate the failure processes of concrete. Subsequently, a large number of random aggregate models, including 2D polygon models [40], 3D ellipsoid models [41], and 3D spherical models [42], have been proposed and implemented to study mesoscopic mechanical properties.

Natural aggregates mixed into concrete always have corner angles and facets, which are difficult to characterize using the aforementioned mesoscale models, but are strongly associated with the mechanical behavior of concrete [43]. Therefore, 3D convex polyhedron models with random aggregate shapes have been established for the characterization of coral aggregates. The overall and localized shape properties of these 3D particle models are controlled by a sphericity value and angularity index. The corresponding generation algorithm is described in detail in Ref. [37]. Fig. 1 presents a comparison of 3D random aggregate models and actual coral aggregates. It can be seen that the irregular shapes and surfaces of coral aggregates can be accurately represented using 3D random aggregate models. The equivalent diameters of these particle models range from 5 to 20 mm, which agrees with the actual aggregate gradations identified in previous studies [28–30].

2.2. Generation of mesoscale models

At the mesoscale level, concrete is typically simplified as a triphase composite, where coarse aggregates are controlled based on four factors of shape, size, content, and spatial localization. As discussed earlier, the random shapes of the aggregates can be accurately represented by the proposed 3D random models. Aggregate size and volume content are determined by concrete grades, which can be described using Fuller's grading curve (Fig. 2). We employ the "take and place" algorithm [39] to place the proposed 3D random aggregate models within the concrete spatial zone. The spatial coordinates of each aggregate model are adjusted and finalized by means of aggregate translation and orientation. Fig. 2 presents a random distribution of aggregate models in a cube specimen with dimensions of 150 mm × 150 mm × 150 mm, where the aggregate size is in the range of 5–20 mm and the aggregate volume is 35%.

To analyze the mechanical properties of concrete numerically, an FEM of concrete composed of three components (coarse aggregate, mortar matrix, and ITZ) must be established. During the meshing process of the 3D random mesoscale models, it is critical to identify each mesoscale component so that the corresponding material attributes and stress–strain behaviors can be defined and characterized. By employing the mapping algorithm and material identification algorithm proposed by Fang et al. [44], 3D mesoscale FEMs were obtained, as shown in Fig. 3, where the minimum mesh size is 1 mm. Based on the size independence of the ITZ thickness identified in our previous study [21], the ITZ thickness has a negligible effect on the numerical results when it is set to 1 to 2 mm. Therefore, the thickness of the ITZ in our 3D random mesoscale model was set to 1 to 2 mm. The cube model with an edge length of 150 mm and cylinder model with dimensions of ϕ150 mm × 300 mm contain 337 500 and 1 725 960 solid elements, respectively. To maintain consistency between the aggregate contents in the mesoscale models and actual CAC specimens reported in Refs. [28–30], where the coarse aggregate volume is in the range of 40%–45%, the aggregate volumes in the cube and cylinder models were set to 42.2% and 43.4%, respectively. The generation processes for the 3D random aggregate models and FEMs were all performed using the ANSYS/LS-DYNA software. To model the failure deformation of concrete, an erosion technique was used to delete elements when the strain exceeded the critical erosion criteria. Based on the results of previous studies [21,30], a maximum principal strain of 0.15 and shear strain of 0.8 were adopted as the erosion criteria for mortar and ITZ, respectively, whereas a maximum principal strain of 0.20 was adopted as the erosion criterion for the coral aggregate.

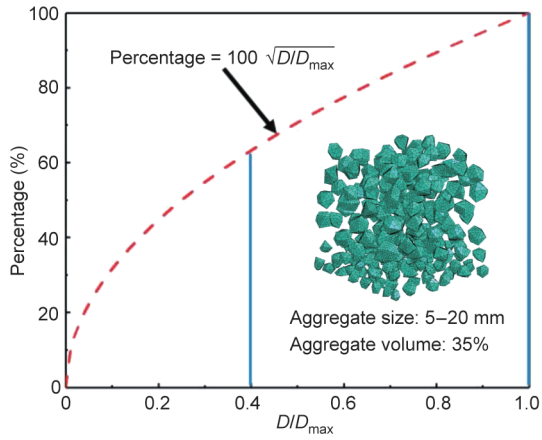

Fig. 2. Fuller's grading curve and coarse aggregate distribution in cube specimen.

In this study, specimen geometry and the width of the load-bearing strips in splitting-tensile tests were considered as influencing factors for the static splitting-tension strength of CAC. According to the specifications for strip width in various setups for the splitting-tensile testing of concrete (Table 1 [7,8,10]), cube and cylinder specimens are typically used for such testing. The width of the load-bearing strip varies from 6 to 25 mm in different standards, corresponding to a relative width ($\beta = b/D$) ranging from 0.04 to 0.17. Therefore, for the cube and cylinder specimens shown in Fig. 3, the strip width is set to 6 to 20 mm (β = 0.04 to 0.13). As shown in Fig. 3, load-bearing strips with different widths are placed symmetrically on the lateral surface of a specimen. Monotonic displacement loading is uniformly applied on the upper strip at a constant loading rate of 7.5 × 10^{-6} m·s^{-1} and the entire splitting-tensile system is constrained by the lower strip.

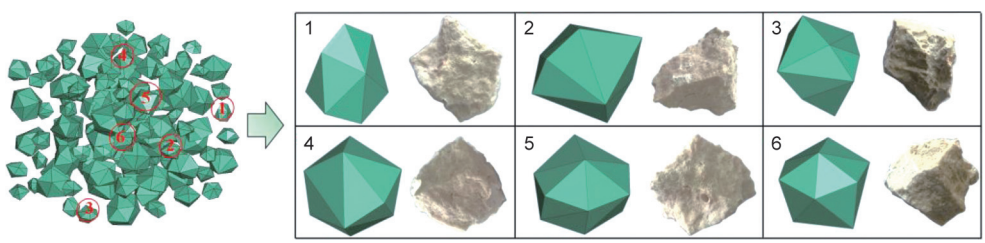

Fig. 1. Comparison of 3D random aggregate models and actual coral aggregates (5–20 mm).

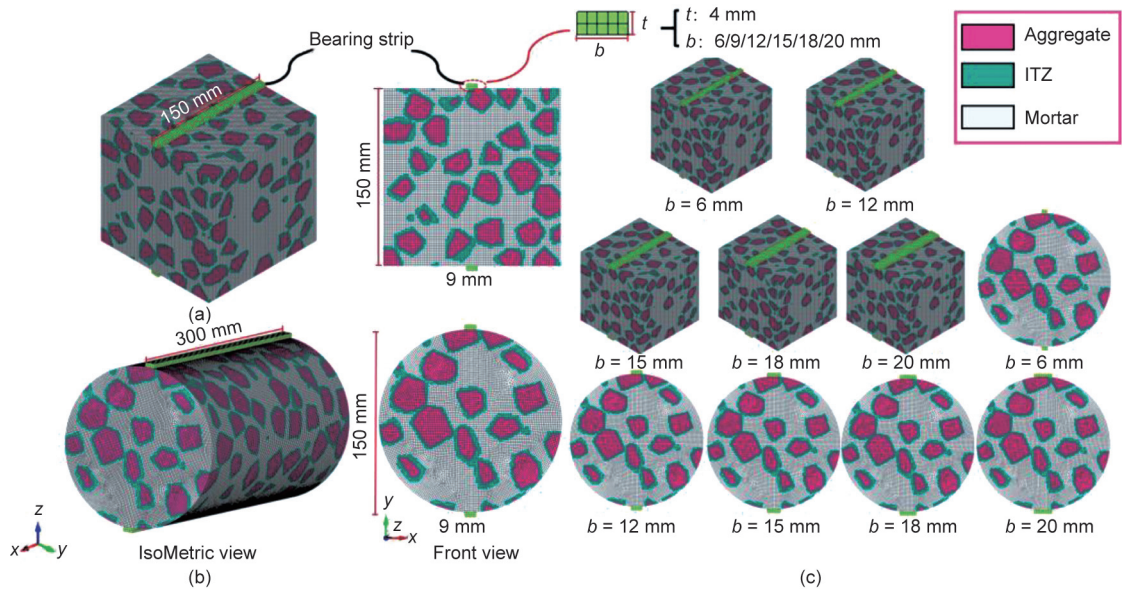

Fig. 3. 3D mesoscale models for CAC having various shapes and strip sizes. (a) Cube model (150 mm × 150 mm × 150 mm); (b) cylinder model (ϕ150 mm × 300 mm); (c) models with various strip widths.

Table 1
Specification for specimen geometry and load-bearing strip in splitting-tensile tests.

Standard number	splitting-tensile specimen			Load-bearing strip	
	Shape	Size (mm)	Slenderness	Width b (mm)	Relative width β
ASTM C496-90 [7]	Cylinder	ϕ150 × 300	2	25	0.17
BS 1881-117 (BS_c150/10) [8]	Cylinder	ϕ150 × 300	2	15 ± 2	0.10
BS 1881-117 (BS_q100/4) [8]	Cube	100 × 100 × 100	1	4 ± 1	0.04
BS 1881-117 (BS_q100/15) [8]	Cube	100 × 100 × 100	1	15 ± 2	0.15
BS 1881-117 (BS_q150/4) [8]	Cube	150 × 150 × 150	1	6 ± 1	0.04
BS 1881-117 (BS_q150/10) [8]	Cube	150 × 150 × 150	1	15 ± 2	0.10
GB/T 50081 [10]	Cube	150 × 150 × 150	1	20	0.13

2.3. Material model and analytical parameters

It is well known that each mesoscale component in concrete has distinctive physical and mechanical properties that are responsible for the heterogeneous characteristics of concrete. In other words, the material attributes of each component significantly influence the mechanical properties of concrete and must be defined in terms of accurate material parameters. Based on previous splitting [45], spalling [46], and direct-tensile [47] simulations of concrete, we can conclude that the Karagozian and Case (K&C) model [48] (MAT_72) is suitable for the mesoscopic simulation of CAC under split tension.

It should be noted that the K&C material model, which includes three failure surfaces, is reliable for describing the plastic behaviors of concrete. The strain rate effects and damage effects of concrete are considered in the K&C model using the dynamic increase factor and damage variable λ, respectively. The expressions and relationships of the three failure surfaces are defined as follows:

$$\Delta\sigma_y = \begin{cases} a_{0y} + P/(a_{1y} + a_{2y}P), & P \geq 0.15f_c \\ 1.35f_t + 3P(1 - 3f_t/f_c), & 0 < P < 0.15f_c \\ 1.35(P + f_t), & P \leq 0 \end{cases} \quad (1)$$

$$\Delta\sigma_m = \begin{cases} a_0 + P/(a_1 + a_2P), & P \geq f_c/3 \\ 1.5/\psi(P + f_t), & 0 < P < f_c/3 \\ 3(P/\eta + f_t), & P \leq 0 \end{cases} \quad (2)$$

$$\Delta\sigma_r = a_{0f} + P/(a_{1f} + a_{2f}P) \quad (3)$$

$$\Delta\sigma = \begin{cases} \eta(\Delta\sigma_m - \Delta\sigma_y) + \Delta\sigma_y & (\text{strain hardening}) \\ \eta(\Delta\sigma_m - \Delta\sigma_r) + \Delta\sigma_r & (\text{strain softening}) \end{cases} \quad (4)$$

where a_0, a_1, a_2, a_{0y}, a_{1y}, a_{2y}, a_{0f}, a_{1f}, and a_{2f} are material constants, f_c is the compressive strength, ψ is a coefficient; $P = -\sigma_{kk}/3$ is the pressure, f_T is the tensile strength, and η is the yield scale factor as a function of the damage variable λ.

$$\lambda = \begin{cases} \int_0^{\bar{\varepsilon}_p} \frac{d\bar{\varepsilon}_p}{\gamma(1+P/f_t)^{s_1}} & P \geq 0 \\ \int_0^{\bar{\varepsilon}_p} \frac{d\bar{\varepsilon}_p}{\gamma(1+P/f_t)^{s_2}} & P < 0 \end{cases}, \quad (5)$$

where $d\bar{\varepsilon}_p = \sqrt{2/3 d\varepsilon_{ij}^p d\varepsilon_{ij}^p}$ is the effective plastic strain increment, $d\varepsilon_{ij}^p$ is the strain increment tensor, s_1 and s_2 are the damage scaling parameters for compression and tension, respectively, and γ is the dynamic increase factor.

Fracture energy in the K&C model can be calculated as the area under the stress–strain curves and is typically expressed as

$$G_f = h \int \sigma d\varepsilon, \quad (6)$$

where G_f is the fracture energy and h is the characteristic length of an element. The pressure softening of concrete under tension and compression is expressed by the volumetric plastic strain $\Delta\lambda = s_3 f_d k_d(\varepsilon_v - \varepsilon_{v,yield})$, where s_3 is a user-defined scalar multiplier,

k_d is an internal scalar multiplier, ε_v is the volumetric strain, $\varepsilon_{v,\,yield}$ is the volumetric strain at yield, and f_d is used to restrict the effects of volumetric damage.

The K&C model was further improved by Malvar et al. [49] by using Release III (*Mat_Concrete_Damage_REL3) to simplify the parameter input process. Therefore, the analytical parameters corresponding to the K&C model parameters for concrete can be generated automatically after inputting some basic parameters, namely the compressive strength f_c, tensile strength f_T, shear modulus G_s, mass density ρ, and Poisson's ratio μ.

According to the physical and mechanical properties of coral aggregates produced by the South China Sea Islands [30,50,51], the material model parameters for the coral aggregate were set to f_c = 10 MPa, f_T = 1.2 MPa, ρ = 2557 kg·m^{-3}, and μ = 0.23. Additionally, by referring to the mechanical properties of coral mortar mixed with different water/cement ratios in Ref. [23], the computational parameters for mortar with a strength grade of C30 were set to f_c = 30 MPa, f_T = 5.6 MPa, ρ = 2350 kg·m^{-3}, and μ = 0.21. Based on the scale limitations of the ITZ (μm), it is difficult to measure its macroscopic properties, particularly the values of f_T and μ. In this study, the bonding strength (3.5 MPa) between a coral aggregate cubic sample (2 cm × 2 cm × 1 cm) and cement paste specimen (2 cm × 2 cm × 1 cm) [30] was used as the tensile strength value for the ITZ in CAC. Additionally, according to the universally acknowledged "weakened mortar" theory [52], the other uncertain parameters of the ITZ, namely f_c, ρ, and μ, were preliminarily set as follows: f_c = 21 MPa, f_T = 3.5 MPa, ρ = 2350 kg·m^{-3}, and μ = 0.15.

2.4. Verification

In this section, the mesh sensitivity of the mesoscale model described above is investigated. Fig. 4 presents the quasi-static splitting-tensile behaviors of CAC cube specimens meshed with different mesh sizes (1, 2, and 3 mm). Fig. 4(a) indicates that the model for static problems is mesh dependent with respect to strain localization because of the lack of a suitable regularization technique. For example, the aggregate and ITZ distributions in a mesoscale concrete model with small grids (1 mm) are more realistic and uniform than those in a model meshed with large grids (2 or 3 mm). Additionally, under quasi-static split tension, the cracking failure patterns of CAC meshed with small elements (1 mm) are more realistic than those of mesoscale models meshed with large elements (2 or 3 mm). Although the shapes of the splitting cracks are similar, the widths of the cracks in the model meshed with smaller elements (1 mm) are smaller and closer to the experimental results [29]. Therefore, 1 mm elements are more suitable for modeling the splitting cracks of concrete. Regarding the load–displacement curves in Fig. 4(b), the peak stress of CAC under split tension is associated with the mesh size. With an increase in mesh size, the peak stress exhibits a slight increase. However, the stress differences between the concrete models with different mesh sizes are small, which is consistent with previous research results [3,21]. Furthermore, based on our previous works [21,44], the optimal mesh size for a 3D random mesoscale model is typically between one-quarter and one-eighth of the minimum aggregate size for the realistic characterization of aggregates and ITZ phases in concrete models. In this study, the mesh size was set to 1 mm, which is one-fifth of the minimum aggregate size (5 mm), which is within the reasonable range for finite element meshes.

The 3D random mesoscale modeling approach and material model parameters for CAC discussed above were verified through comparisons of numerical simulation results and test results reported in the literature [29,53,54]. A 3D cube mesoscale model with an edge length of 100 mm and an aggregate volume of 43.2% was established to simulate the C40CAC cubes with the same specimen size and similar aggregate volume (45.5%) used in Mi et al.' s [29] splitting-tensile tests. Crushed coral aggregates with a continuous gradation of 5 to 20 mm were used in Mi et al.'s tests and the coarse coral aggregates in our mesoscale model were simulated using 3D random aggregate models (Fig. 1) within the size range of 5–20 mm. The width of the load-bearing strip was 20 mm. The tested and simulated failure patterns of CAC under split tension are presented in Figs. 5(a) and (b), respectively.

According to the test results [29] shown in Fig. 5(a), the main cracks appear at the central plane of the cube specimen. Additionally, clear compressive failure occurs at the loading position, which is caused by the concentrated stress distribution between the load-bearing strip and specimen. One can see that the splitting-tensile fracture surface meanders through the specimen near the central plane based on the heterogeneity of concrete, which is very consistent with the experimental cracking pattern presented in Fig. 5(a). The concentrated stress distribution and localized cracking failure near the loading position were also simulated, as shown in Fig. 5(b). Apparent cracking failure of the coral aggregates can be observed on the fracture surfaces of the concrete specimen, as shown in Fig. 5(a). Da et al. [28] and Ma et al. [30] observed the same failure mode of coral aggregates in their experimental works and attributed this failure to the highly porous and low-strength characteristics of coral aggregates. It is noteworthy that both the spatial location and cracking phenomenon of coral aggregates in CAC can be simulated accurately using the proposed mesoscale

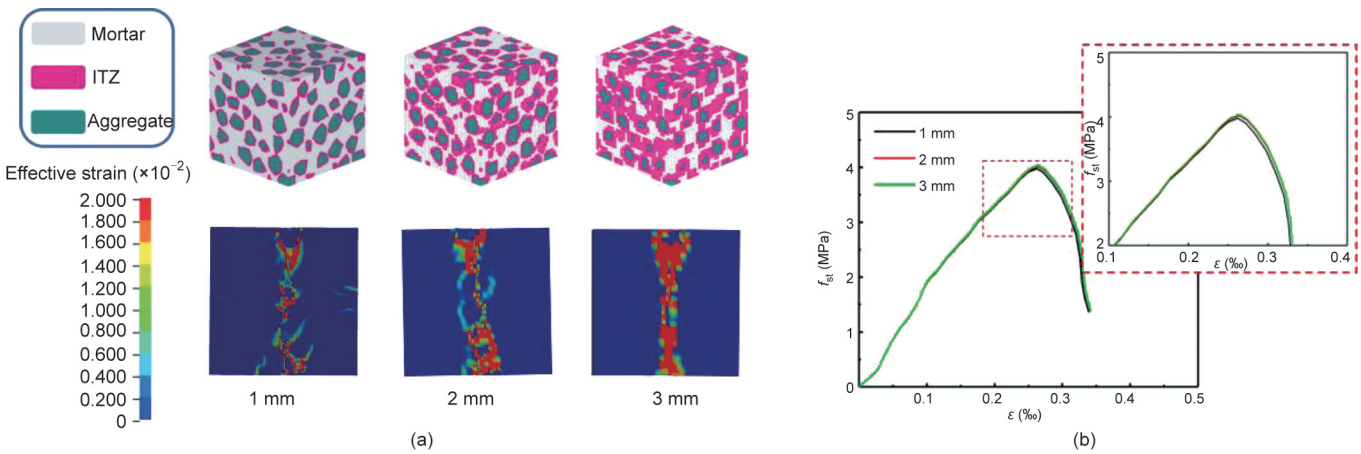

Fig. 4. Mesh sensitivity effect on the splitting-tensile simulations of cube CAC specimens. (a) Failure patterns; (b) stress–strain curves.

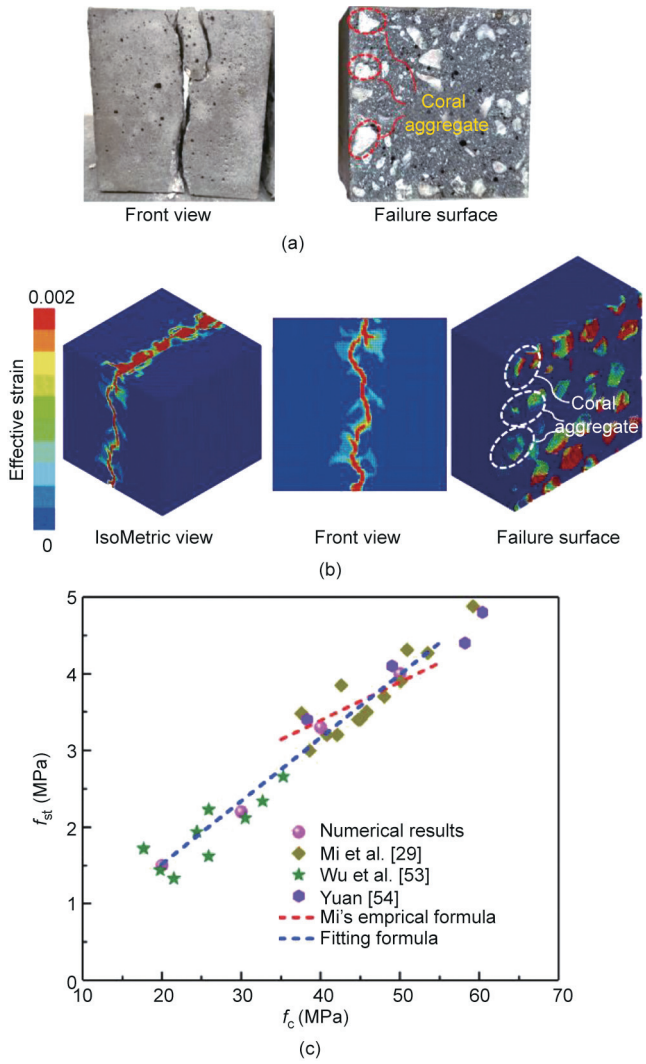

Fig. 5. Comparison of experimental and numerical results of CAC under static split tension: (a) tested failure pattern; (b) numerical failure pattern; and (c) static spitting-tensile strengths.

model, as shown in Fig. 5(b). This indicates that the mesoscale model and material model are suitable for the simulation of CAC under split tension. Additionally, according to the comparisons of the relationships between splitting-tensile strength (f_{st}) and the f_c values of cube CAC specimens in Ref. [29], a reliable fitting formula can be obtained, as shown by the dotted blue line in Fig. 5(c) [53,54]. One can see that the f_{st} values of CAC cubes with various f_c values (20 to 40 MPa) can be predicted from the correlation curve fitted to the test results, indicating that the 3D random mesoscale modeling approach and corresponding model parameters are highly reliable for simulating the mechanical properties of CAC under split tension.

Similarly, using the same mesoscale model and model parameters, a comparison of numerical and experimental results, in terms of failure patterns and stress–strain curves, for CAC under quasi-static uniaxial compressive loads is presented in Fig. 6. As shown in Fig. 6(a), the experimental failure patterns of CAC under uniaxial compression presented in Ref. [29] can be accurately simulated using the proposed 3D mesoscale model, where the strain rate is set to 10^{-5} s^{-1} and the friction effects on the upper and lower surfaces of the specimen are not considered. Additionally, by comparing the compressive stress–strain curves of CAC presented

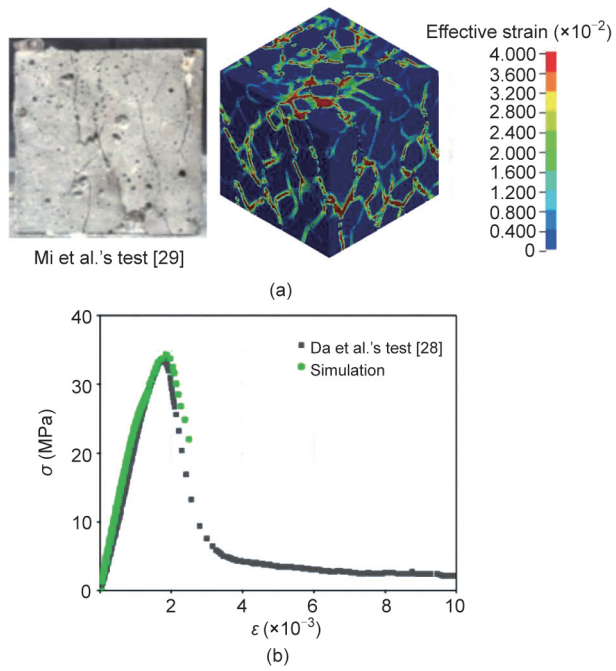

Fig. 6. Comparison of experimental and resunumericallts of CAC under static split tension: (a) compressive failure patterns; and (b) compressive stress–strain curve.

in Fig. 6(b), one can see that the numerical curve is in good agreement with the test curve [28]. In summary, the developed 3D mesoscale modeling approach has high reliability for simulating the mechanical responses of CAC under different load conditions. Therefore, the developed FEM and analytical parameters discussed in the previous sections were employed in the numerical analysis discussed below.

3. Mesoscopic results and discussion

The mesoscopic properties of CAC were obtained based on the mesoscale models described above. The results are discussed in this section. The failure processes, final failure patterns, and stress–displacement relationships of different CAC specimens are analyzed and the specimen geometry (cube and cylinder) and width of the load-bearing strip (6, 9, 12, 15, 18, and 20 mm) are considered as influencing factors.

3.1. Failure processes

To evaluate the failure mechanisms of CAC under spilt tension, the overall and localized failure processes of the cube and cylinder CAC models are presented in Figs. 7 and 8, respectively, where load-bearing strips with widths of 9 mm are used. As shown in Figs. 7(a) and 8(a), both the cube and cylinder models are cut through their central planes along the loading direction to investigate localized failure processes.

As shown in Figs. 7(b) and 8(b), strain concentrations appear at the upper loading ends between the specimens and strips, and then gradually propagate along the loading direction through the central plane. Subsequently, the strain-concentration phenomenon occurs at the lower loading end and propagates along the loading diameter direction toward the upper loading end until the upper and lower splitting cracks meet and connect at the specimen center, splitting the specimen into two halves. In addition to the main cracks with large widths that split the specimen into two halves, some secondary cracks also occur in the area near the loading

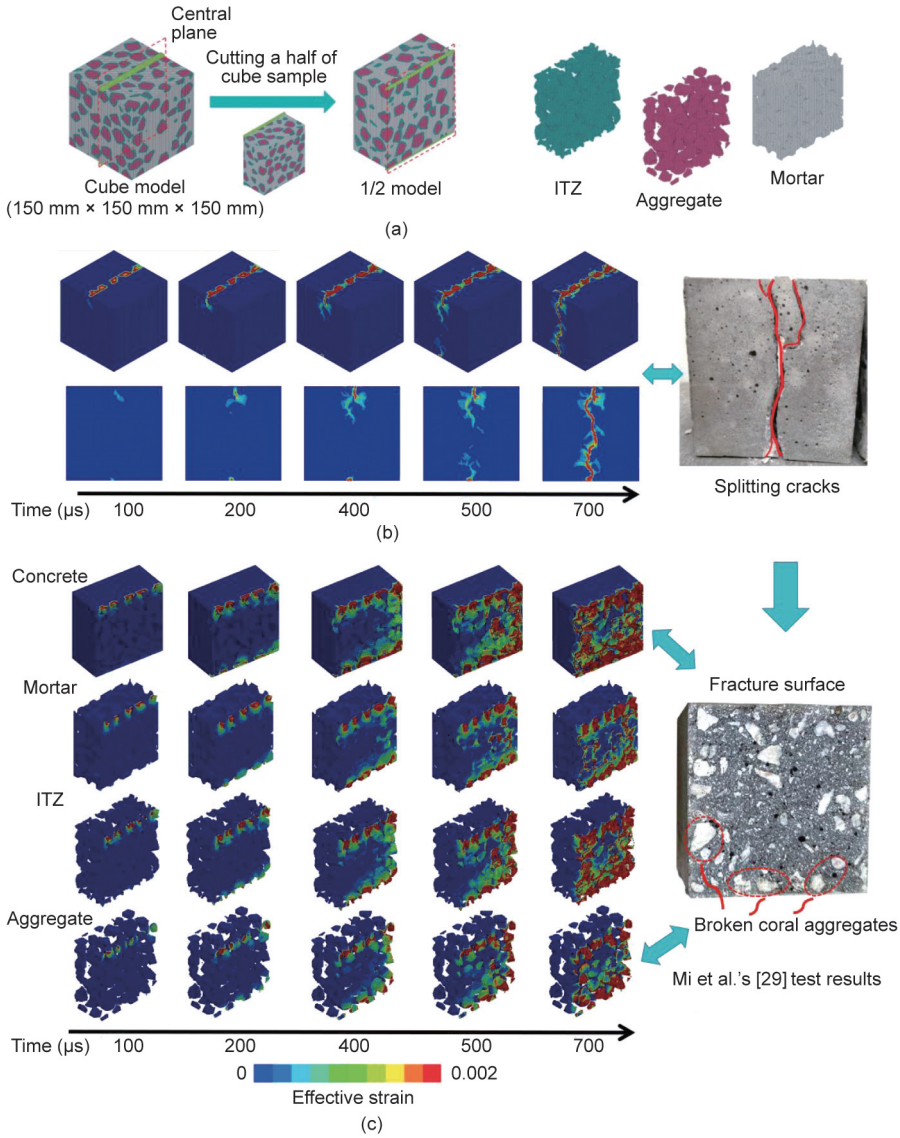

Fig. 7. Failure process of cubic CAC specimen under split tension [29].

position (Fig. 7(b)), which is likely caused by the appearance of aggregates along the central plane. In summary, the numerical crack patterns of CAC under split tension are highly consistent with the test results presented by Mi et al. [29] and Ma et al. [30], as shown in Figs. 7 and 8. However, the crack propagation originating from the upper loading end is faster than that originating from the lower loading end, which can explain the actual failure behavior of CAC under split tension. When comparing the failure processes of the cube and cylinder, the strain concentration area in the cylinder is wider than that in the cube, which can be attributed to the smaller elastic plastic strain range (0–0.001) of the cylinder. The main purpose of setting a smaller elastic plastic strain range for the cylinder is to highlight its failure process, but its failure speed is clearly slower than that of the cube specimen based on its larger fracture surface.

The failure process of CAC under static split tension can be derived from the localized failure characteristics (Figs. 7(c) and 8(c)) of concrete. It should be noted that the strain concentration of the ITZ is much more significant than that of the mortar and aggregate based on the lower tensile strength of the ITZ, which leads to easy micro-crack initiation and propagation through the ITZ [29,53,54,60]. It should also be noted in the test results presented by Mi et al. [29] and Ma et al. [30] (Figs. 7 and 8) that the fracturing of coral aggregates appears on the splitting failure surfaces of both the cube and cylinder CAC specimens, demonstrating that cracks can pass and even penetrate coral aggregates under quasi-static loading. By using the mesoscale modeling approach, stress initiation, propagation, and concentration in coral aggregates can be accurately simulated based on the variation of effective strain, as shown in Figs. 7(c) and 8(c). According to previous experimental and numerical studies, the fracturing of coral aggregates in CAC is attributed to two main factors. One is that coral aggregates are porous and lightweight aggregates with low strength that cannot bear large tensile loads [27–30]. The other is that the rough and porous surface textures of coral aggregates can contribute to an ITZ with high bonding intensity and strength, which gives rise to internal cracking failures that tend to propagate through and penetrate coral aggregates with porous mesostructures [53,54]. Additionally, based on the failure processes of internal mesoscale components shown in Figs. 7(c) and 8(c), it can be concluded that damage in concrete develops from the edge areas of specimens toward the centers of the specimens and that the failure of mesoscale components in edge areas is more significant than that in central areas, which can be attributed to the heterogeneity

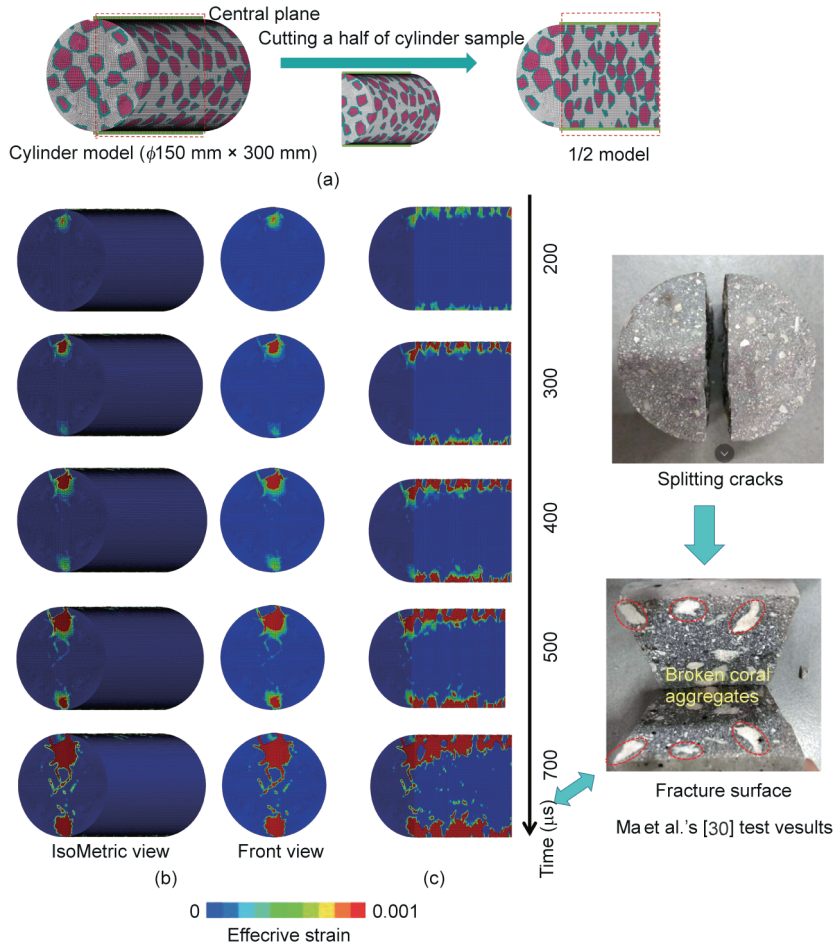

Fig. 8. Failure process of cylinder CAC specimen under split tension [30]. (a) Overall and localized model; (b) overall failure process; (c) localized failure process.

of concrete and is consistent with the simulation results presented by Jin et al. [3].

3.2. Final failure patterns

Fig. 9 presents the final failure patterns of the cube/cylinder CAC specimens subjected to static splitting-tensile loadings, where the width of the load-bearing strip varies from 6 to 20 mm. As shown in Fig. 9, under static splitting-tensile loading, both the cube and cylinder specimens are split into two halves along their central loading planes. A damage belt with a certain width exists near the fracture zone, which is induced by compressive and tensile loading in the transverse direction. One can see that the width of both the damage belt and cracking path of CAC are associated with the load-bearing strip width. For example, with an increase in strip width, the damage belt width gradually increases and ribbon cracking failure in the specimen centers can be detected. This phenomenon can be attributed to the fact that the loading area gradually increases with an increase in strip width, which gives rise to compressive stress concentrations at the contact area between the specimen and load-bearing strip. Therefore, compressive failure with a greater width occurs at the contact area for a specimen with a large strip, which is consistent with Zhou et al.'s [55] summarizations of the representative failure patterns of concrete under split tension. However, it should be noted that the failure of CAC subjected to wider loading combines both compressive and tensile failure, where compressive failure accounts for the majority of damage. In other words, in splitting-tensile tests of concrete specimens, the main failure mode of specimens with wide strips is compressive failure, rather than pure splitting-tensile failure, which can lead to the overestimation of the splitting-tensile strength of concrete. Additionally, bending-tensile failures occurred on the two lateral surfaces of the cube CAC specimen, which were parallel to the loading plane when the strip width was greater than 18 mm. Jin et al. [3] also observed this phenomenon in a cube mesoscale model subjected to splitting-tensile loading.

3.3. Load–displacement results

To analyze the effect of load-bearing strip width on the splitting-tensile strength of CAC specimens, the relationships between the load (L) and horizontal displacement (δ) of the cube and cylinder specimens are plotted in Figs. 10(a) and (b), respectively. In our numerical analysis, δ was calculated as the average displacement between the two opposing surfaces that were parallel to the loading direction. As shown in Fig. 10, the splitting load on the CAC specimens in the simulations gradually increases with the horizontal displacement and exhibits a decreasing trend when the peak load is achieved. The enhancement process of the splitting load fluctuates based on the low strength and high porosity of CAC. Additionally, for both the cube and cylinder specimens, a clear increasing trend in the peak load and corresponding displacement of the CAC can be observed as the strip width increases. Based on the ascending section of the load–displacement curves (Fig. 10), it can be concluded that the greater the strip width, the greater

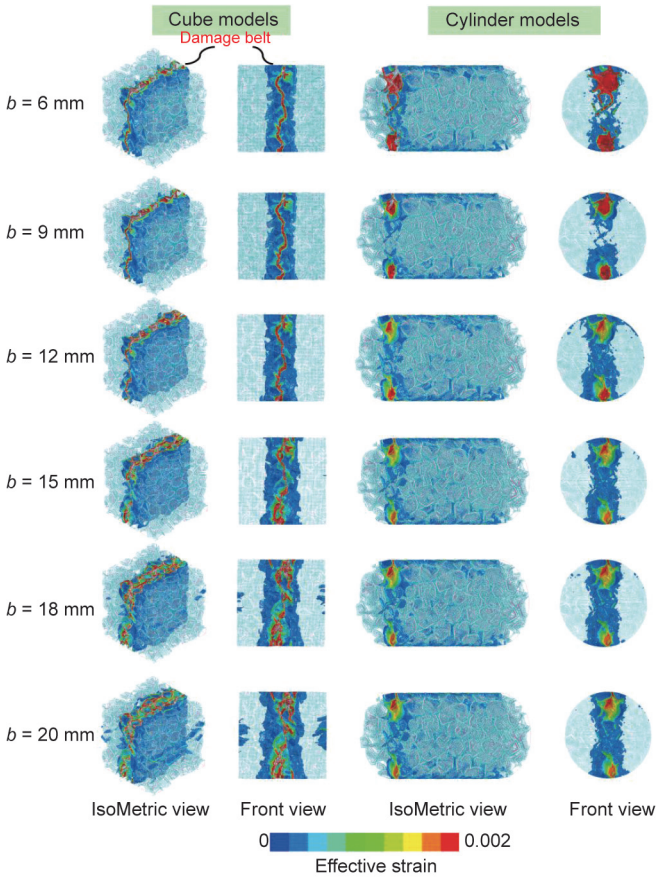

Fig. 9. Final failure patterns of cube and cylinder CAC specimens under split tension.

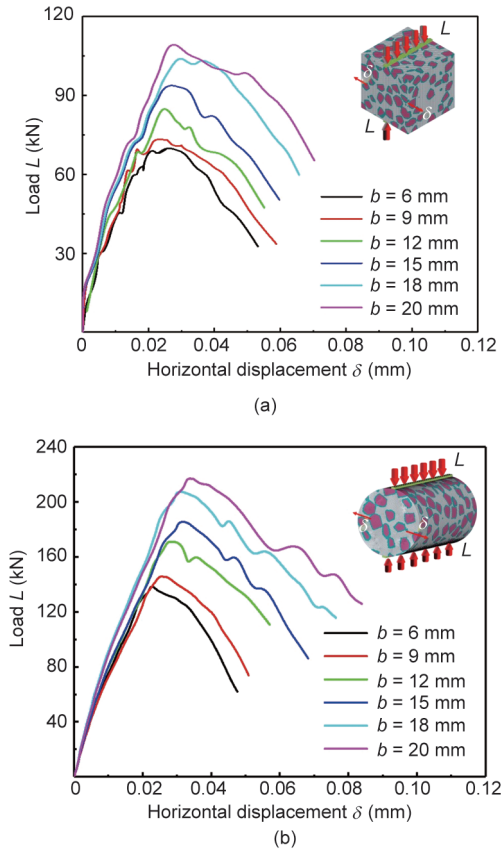

Fig. 10. Load-displacement curves of CAC specimens with various bearing strip sizes: (a) cube specimens and (b) cylinder specimens.

the stiffness of the CAC specimen. Compared to the softening curves of the CAC specimens with narrow strips, it can be observed that the softening curves of the CAC specimens with wide strips fluctuate with increasing displacement, indicating that re-hardening phenomena occur in the specimens. This is because localized compression plays a more significant role in CAC specimens with wider strips. As indicated in many previous studies [13,19,56], there is a direct relationship between the width of the bearing strip and the splitting-tensile strength of concrete, which is analyzed and discussed in the following sections.

4. Effects of specimen geometry and bearing strip size on tensile strength

Based on the obtained numerical results and available test results for the splitting-tensile strengths of CAC specimens, the effects of specimen geometry and strip width on tensile strength are discussed in this section. The splitting-tensile strengths of the cube and cylinder specimens were obtained when the specimens were split in half by horizontal tensile stress. The failure of the wedges considered in this work is included in the failure processes of concrete (Fig. 8), but tensile strength cannot be obtained in the event of wedge failure.

4.1. Splitting-tensile strength

The peak loads of CAC specimens under different conditions according to the load–displacement curves presented in Fig. 10 are listed in Table 2. We used the classical formula (Eq. (7)) for the splitting-tensile strength of concrete to calculate the f_{st} value of CAC (Table 2). Considering differences in specimen geometry and size, the relative width (β) of the load-bearing strip was determined using Eq. (8) to quantify the relationship between f_{st} and the strip width.

$$f_{st} = \frac{2L}{\pi HD} \tag{7}$$

$$\beta = b/D \tag{8}$$

where f_{st} represents the splitting-tensile strength (MPa), L is the peak load (kN), b is the width of the load-bearing strip, H is the height and edge length of the cylinder and cube specimens, respectively, and D is the diameter and edge length of the cylinder and cube specimens, respectively.

4.2. Effects of specimen geometry on tensile strength

Fig. 11 plots the numerical f_{st} values of the cube and cylinder CAC specimens with various load-bearing strip widths (6 to 20 mm). One can see that the f_{st} value obtained for the cylinder model (ϕ150 mm × 300 mm) is slightly smaller than that of the cube model with an edge length of 150 mm when the load-bearing strip widths are the same. On the surface, it appears that the f_{st} values obtained using different standards (i.e., ASTM C496-90 [7], BS 1881-117 [8], and GB/T50081 [10]) are influenced by the specimen geometry to a certain degree. However, based on the failure positions of splitting-tensile specimens, many researchers [58,59] have suggested specifying the relationship between concrete tensile strength and the fracture areas of specimens to investigate specimen size effects, independent of specimen geometry. In other words, both specimen size (volume) and specimen

Table 2
Splitting-tensile strengths of CAC with various geometries and load-bearing strip widths.

Specimen geometry	Specimen size (mm × mm × mm)	Splitting area (mm^2)	b (mm)	β	L (kN)	f_{st} (MPa)
Cube	150 × 150 × 150	22 500	6	0.04	70.2	1.99
	150 × 150 × 150	22 500	9	0.06	73.9	2.09
	150 × 150 × 150	22 500	12	0.08	86.8	2.46
	150 × 150 × 150	22 500	15	0.10	94.2	2.67
	150 × 150 × 150	22 500	18	0.12	105.4	2.98
	150 × 150 × 150	22 500	20	0.13	110.5	3.13
Cylinder	ϕ150 × 300	45 000	6	0.04	138.6	1.94
	ϕ150 × 300	45 000	9	0.06	145.8	2.08
	ϕ150 × 300	45 000	12	0.08	171.2	2.40
	ϕ150 × 300	45 000	15	0.10	185.6	2.62
	ϕ150 × 300	45 000	18	0.12	207.5	2.94
	ϕ150 × 300	45 000	20	0.13	217.4	3.08

Based on the suggestion in Ref. [57], the splitting area of the concrete specimen under split tension is simplified as the vertical cross-sectional area along the loading direction.

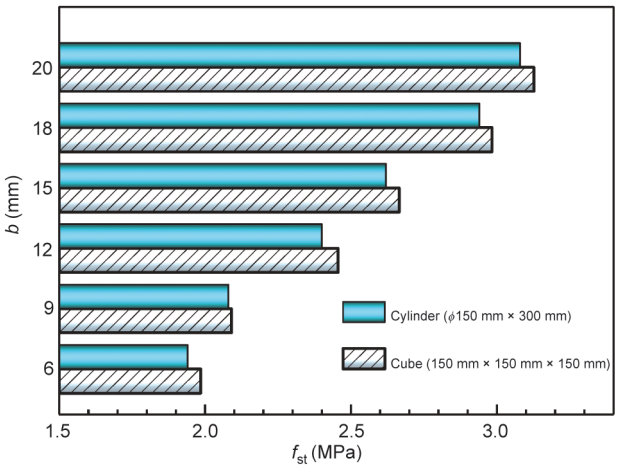

Fig. 11. The numerical f_{st} values of CAC with various specimen geometries.

geometry (shape) are considered to be of general significance for the f_{st} values of concrete. Therefore, the relationships between the fracture areas and f_{st} values of simulated CAC specimens are presented in Fig. 12(a).

As shown in Fig. 12(a), the f_{st} values of CAC exhibit a decreasing trend as the fracture area increases from 225 to 450 cm^2. Kadleček et al. [57] also observed varying trends in the f_{st} values of OPC with various specimen geometries and sizes with a strip width of one-tenth of the diameter or edge length of each specimen. Specifically, the f_{st} values of cube and cylinder OPC specimens gradually decrease as the fracture area increases from 16 to 450 cm^2, indicating that f_{st} is size dependent in terms of the fracture area. Additionally, when comparing the f_{st} value of a cube OPC specimen with edge lengths of 100 mm (150 mm) to that of a cylinder specimen with dimensions of ϕ100 mm × 200 mm (ϕ150 mm × 300 mm), the strength difference is similar to that of CAC specimens with the same geometries. Therefore, we can conclude that the numerical results for CAC specimens with different shapes and strip widths are reasonable and that the 3D random mesoscale modeling approach is practical for investigating the static f_{st} values of CAC. The detailed relationships between the fracture areas and f_{st} values of CAC will be explored quantitatively in future work.

4.3. Effects of bearing strip width on tensile strength

Several studies have reported that the f_{st} value of concrete is directly dependent on the width of the load-bearing strip when the relative width of the load-bearing strip is greater than 4% [19]. Fig. 13 presents the variation in the numerical and test f_{st} values of CAC and OPC [60] with the relative widths of the load-bearing strip [29,53,54,60]. It should be noted that the f_{st} value of CAC gradually increases with the relative width of the strip, which is consistent with the trend of the OPC [60]. Additionally, when the relative width of the strip is less than 0.08, there is a slight difference between the f_{st} value of CAC and the OPC value reported by Olesen et al. [60]. This gap gradually increases, indicating that the f_{st} value of CAC tends to be greater than that of OPC, which is consistent with the results of Mi et al.'s [29] splitting-tensile tests

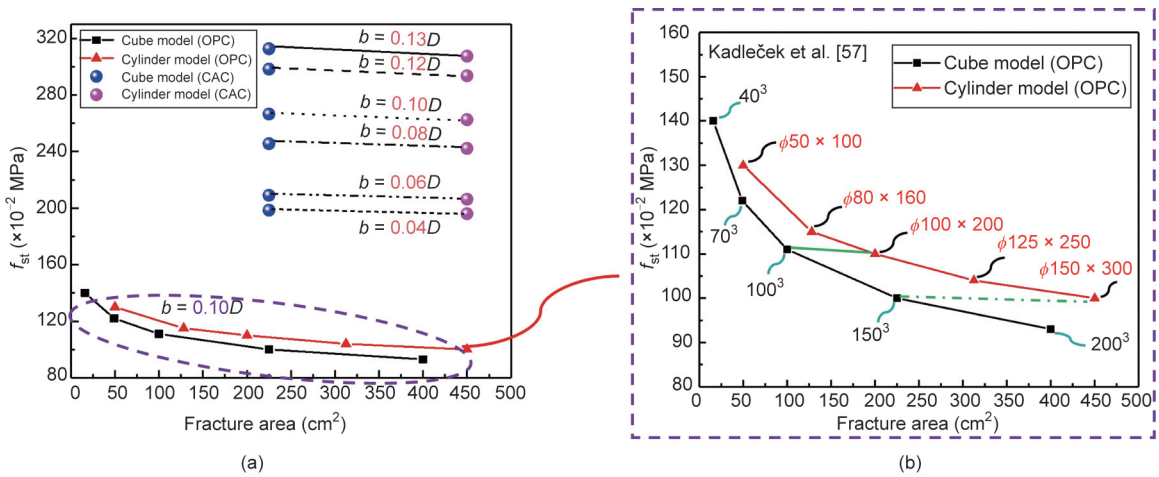

Fig. 12. The relations between f_{st} and fracture area of CAC with various specimen geometries.

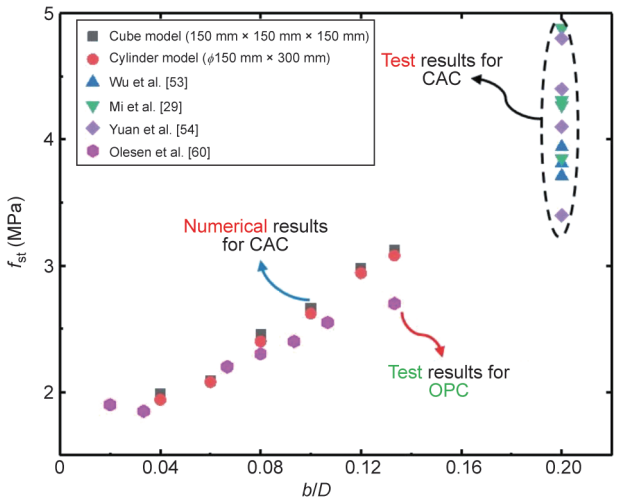

Fig. 13. Static splitting-tensile strength of CAC and OPC specimen with various shapes and load-bearing strip widths.

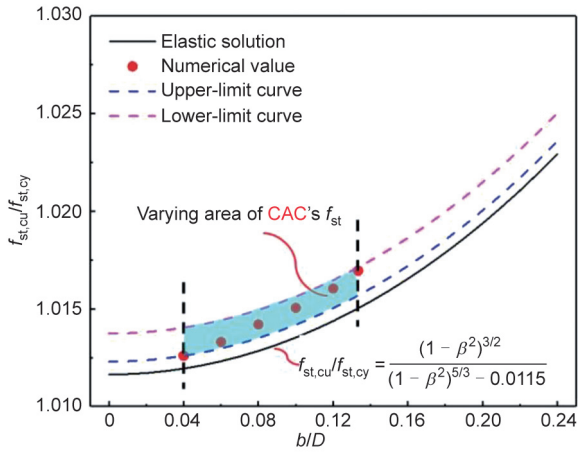

Fig. 14. Relations between cube/cylinder splitting-tensile strength and the relative width of bearing strip.

of CAC and OPC. They explained that this phenomenon is caused by strong mechanical interlocking between mortar and coral aggregates with rough surface textures, which contributes to the bonding strength of the ITZ and increases the f_{st} value of CAC compared to OPC, which contains gravel aggregates. Additionally, when the relative width of the strip is 0.20, one can see that the test f_{st} values of CAC fluctuate, which is attributed to the fact that the CAC specimens discussed in Refs. [29,53,54] have distinct compressive strengths (30 to 60 MPa).

The classical formula (Eq. (7)) for the calculation of f_{st} is based on the linear-elastic solution method, where the splitting load on the upper strip is uniformly distributed along a line with no width, which is inaccurate when a wide bearing strip is used to carry a portion of the compressive stress. Therefore, considering the effects of the relative width of the bearing strip, Rocco et al. [13] calculated the f_{st} values of cube and cylinder specimens using Eqs. (9) and (10), respectively.

$$f_{st,cu} = f_{st}\left[(1-\beta^2)^{5/3} - 0.0115\right]^{-1} \tag{9}$$

$$f_{st,cy} = f_{st}(1-\beta^2)^{-3/2} \tag{10}$$

where $f_{st,cu}$ and $f_{st,cy}$ are the splitting-tensile strengths of the cube and cylinder specimens, respectively. Therefore, the relationship between the f_{st} values of the cube and cylinder specimens under the same conditions can be expressed as follows [19]:

$$\frac{f_{st,cu}}{f_{st,cy}} = \frac{(1-\beta^2)^{3/2}}{(1-\beta^2)^{5/3} - 0.0115} \tag{11}$$

When comparing the ratio of the numerical $f_{st,cu}$ and $f_{st,cy}$ values of CAC to that of the elastic solutions (Eq. 11) (Fig. 14), one can see that the numerical ratio of CAC is greater than that of the elastic solutions. Additionally, one can see that the differences between $f_{st,cu}$ and $f_{st,cy}$ gradually increase as the relative width of the bearing strip increases from 0.04 to 0.13, which is faster than the rate of increase of the elastic solution. In other words, the effects of specimen geometry on the f_{st} value of CAC become more significant with an increase in the relative width of the bearing strip. The main reason for these differences between the numerical and elastic solutions is that the width of the splitting load gradually increases with the relative width of the bearing strip, which is inconsistent with the assumption of a linear load with no width. The larger the relative width of the bearing strip, the greater the difference between the numerical and theoretical results.

Therefore, based on the elastic solution method, the effects of other factors on the ratio of $f_{st,cu}$ and $f_{st,cy}$ for CAC with different bearing strip widths can be represented by the following upper and lower limit formulas:

Upper limit formula

$$\frac{f_{st,cu}}{f_{st,cy}} = \frac{(1-\beta^2)^{3/2}}{(1-\beta^2)^{5/3} - 0.0115} + K_1 \tag{12}$$

Lower limit formula

$$\frac{f_{st,cu}}{f_{st,cy}} = \frac{(1-\beta^2)^{3/2}}{(1-\beta^2)^{5/3} - 0.0115} + K_2 \tag{13}$$

where K_1 and K_2 are constants that control the upper and lower boundaries of the variation area of CAC f_{st} values, respectively. Both equations are valid for β = 0.04 to 0.13. According to the numerical $f_{st,cu}$ and $f_{st,cy}$ values of CAC with different bearing strip widths, K_1 and K_2 are preliminarily determined as 2.1×10^{-4} and 6.6×10^{-4}, respectively. However, additional numerical and test $f_{st,cu}$ and $f_{st,cy}$ values for CAC under split tension with various bearing strip widths are required for the further determination of K_1 and K_2. Overall, the upper and lower limit formulas are of great significance for predicting the f_{st} values of CAC with different bearing strip widths, which has massive implications for the investigation and design of CAC structures.

5. Conclusions

The splitting-tensile properties of cubic and cylindrical CAC specimens were investigated using a 3D random mesoscale modeling approach. The effects of specimen geometry and the width of the bearing strip on the f_{st} value of CAC were studied based on numerical results and previous test results. The main conclusions can be summarized as follows.

(1) A 3D mesoscale model with random characteristics (shapes and distributions) for aggregates was developed to simulate CAC cube and cylinder samples. The proposed mesoscale models and corresponding material parameters for CAC were validated through simulations and by analyzing the mechanical properties of cube and cylinder CAC specimens under split tension.

(2) In the splitting-tensile failure process of CAC, cracking propagates from both the upper and lower bearing strips along the loading direction until the specimen is split into halves by vertical splitting cracks. Additionally, earlier and more rapid cracking

initiates at the upper bearing strip compared to the lower strip, which can explain the real-world failure behavior of CAC under split tension.

(3) The typical failure pattern for CAC is single splitting crack formation along the loading direction. However, when the width of the bearing strip exceeds a certain threshold, multiple ribbon failures occur near the central plane of a CAC specimen.

(4) The numerical f_{st} value of a CAC cube model (150 mm × 150 mm × 150 mm) is slightly greater than that of a similar CAC cylinder model (ϕ150 × 300 mm) and the effects of specimen geometry can be revealed based on the relationship between f_{st} and the fracture area of a specimen. Specifically, the f_{st} value of CAC decreases with an increase in fracture area, which is similar to the results for OPC reported in Ref. [57].

(5) The numerical f_{st} value of CAC is size dependent in terms of the width of the load-bearing strip and it gradually increases with the relative width of the strip, which is consistent with the variation law of OPC. Additionally, based on the elastic solution for the ratio of $f_{st,cu}$ and $f_{st,cy}$, the upper and lower boundaries for the ratio of $f_{st,cu}$ and $f_{st,cy}$ for CAC were determined using Eqs. (12) and (13), which is highly significant for investigating and predicting the splitting-tensile strength of CAC. Additional numerical and test results for CAC should be derived to complement and perfect these formulas in future work.

Acknowledgments

The authors acknowledge financial support from the National Natural Science Foundation of China (52178190, 51878350, 11832013, 51678304, and 52078250), the Science and Technology on Near-Surface Detection Laboratory pre-research Fund (6142414200505), and the Interdisciplinary Innovation Foundation for Graduates, Nanjing University of Aeronautics and Astronautics (NUAA) Grant (KXKCXJJ202005). The support provided by the China Scholarship Council (202006830096) during a visit of Zhangyu Wu to University College London is also sincerely acknowledged. We also sincerely thank the reviewers for their insightful suggestions.

Compliance with ethics guidelines

Zhangyu Wu, Jinhua Zhang, Hongfa Yu, Qin Fang, Haiyan Ma, and Li Chen declare that they have no conflict of interest or financial conflicts to disclose.

Data availability

The data used to support the findings of this study are available from the corresponding author upon reasonable request.

References

[1] Wright PJF. Comments on an indirect tensile test on concrete cylinders. Mag Concr Res 1955;7(20):87–96.
[2] Guo Y, Gao G, Jing L, Shim VPW. Quasi-static and dynamic splitting of high-strength concretes-tensile stress–strain response and effects of strain rate. Int J Impact Eng 2019;125:188–211.
[3] Jin L, Yu W, Du X, Yang W. Mesoscopic numerical simulation of dynamic size effect on the splitting-tensile strength of concrete. Eng Fract Mech 2019;209:317–32.
[4] Chen X, Ge L, Zhou J, Wu S. Dynamic Brazilian test of concrete using split Hopkinson pressure bar. Mater Struct 2017;50:1.
[5] Heilmann HG. Relations between tensile and compressive strength of concrete. Beton 19(2): 68–70. German.
[6] Carneiro FL, Barcellos A. Tensile strength of concrete. RILEM Bull 1949;13:98–125. French.
[7] ASTM C496-90. Standard test method for splitting tensile strength of cylindrical concrete specimens. West Conshohocken: ASTM International; 1990.
[8] BS 1881-117. Testing concrete—part 117: method for the determination of tensile splitting strength. British Standard. London: British Standards Institution; 1983.
[9] Iso 4108. Concrete determination of tensile splitting strength of test specimen. ISO standard. Geneva: International Organization for Standardization; 1980.
[10] GB/T 50081. Standard for test method of mechanical properties on ordinary concrete. Chinese standard. Beijing: China Architecture and Building Press; 2019.
[11] Nilsson S. The tensile strength of concrete determined by splitting tests on cubes. RILEM Bull 1961;11:63–7.
[12] Ince R. Determination of concrete fracture parameters based on peak-load method with diagonal split-tension cubes. Eng Fract Mech 2012;82:100–14.
[13] Rocco CG, Guinea GV, Planas J, Elices M. The effect of the boundary conditions on the cylinder splitting strength. In: Fracture Mechanics of Concrete Structures. Freiburg: Aedificatio Publishers; 1995. p. 75–84.
[14] Zhou H, Che Y, Chen G, Song Y. Size effect on tensile strength of concrete cubes and cylinders. Concrete 2010;8:13–5. Chinese.
[15] Davies J, Bose D. Stress distribution in splitting test. ACI J Proc 1968;65 (8):662–9.
[16] Tang T. Effects of load-distributed width on split tension of unnotched and notched cylindrical specimens. J Test Eval 1994;22(5):401–9.
[17] Rocco C, Guinea GV, Planas J, Elices M. Size effect and boundary condition in the Brazilian tests: theoretical analysis. Mater Struct 1999;32(6):437–44.
[18] Rocco C, Guinea GV, Planas J, Elices M. Size effect and boundary condition in the Brazilian tests: experimental verification. Mater Struct 1999;32(3):210–7.
[19] Rocco C, Guinea GV, Planas J, Elices M. Review of the splitting-test standards from a fracture mechanics point of view. Cement Concr Res 2001;31(1):73–82.
[20] Wu Z, Yu H, Ma H, Zhang J, Da B, Zhu H. Rebar corrosion in coral aggregate concrete: determination of chloride threshold by LPR. Corros Sci 2020;163:108238.
[21] Wu Z, Zhang J, Yu H, Ma H, Chen L, Dong W, et al. Coupling effect of strain rate and specimen size on the compressive properties of coral aggregate concrete: a 3D mesoscopic study. Compos Part B Eng 2020;200:108299.
[22] Lorman WK. Characteristics of coral aggregate from selected locations in the Pacific Ocean area. Report. Port Hueneme: USN Civil Engineering Laboratory; 1958. Report No.: TN-335A.
[23] Lorman WK. Characteristics of coral mortars. Report. Port Hueneme: US Naval Civil Engineering Laboratory; 1960. Report No.:TR-041.
[24] Lorman WK. Coral and Coral Concrete. Report. Port Hueneme: US Naval Civil Engineering Laboratory; 1960. Report No.: TR-068.
[25] Scholer CH. Examination and study of certain structures in the Pacific Ocean area. Report. Port Hueneme: US Naval Civil Engineering Laboratory. 1959. Report No.: NBy-3171.
[26] Howdyshell PA. The use of coral as an aggregate for Portland cement concrete structures. Report. Urbana-Champaign: US Army Construction Engineering Research Laboratory; 1974.
[27] Yu H, Da B, Ma H, Zhu H, Yu Q, Ye H, et al. Durability of concrete structures in tropical atoll environment. Ocean Eng 2017;135:1–10.
[28] Da B, Yu H, Ma H, Tan Y, Mi R, Dou X. Experimental investigation of whole stress–strain curves of coral concrete. Constr Build Mater 2016;122:81–9.
[29] Mi R, Yu H, Ma H. Study on the mechanical property of the coral concrete. Ocean Eng 2016;34:48–54.
[30] Ma H, Wu Z, Zhang J, Yue C. Experimental and three-dimensional mesoscopic investigation of coral aggregate concrete under dynamic splitting-tensile loading. Mater Struct 2020;53(1):12.
[31] Suchorzewski J, Tejchman J, Nitka M, Bobiński J. Meso-scale analyses of size effect in brittle materials using DEM. Granul Matter 2019;21:9.
[32] Skarżyński L, Nitka M, Tejchman J. Modelling of concrete fracture at aggregate level using FEM and DEM based on x-ray μCT images of internal structure. Eng Fract Mech 2015;147:13–35.
[33] Zhou X, Hao H. Mesoscale modelling of concrete tensile failure mechanism at high strain rates. Comput Struc 2008;86(21–22):2013–26.
[34] Schlangen E, Van Mier JGM. Experimental and numerical analysis of micromechanisms of fracture of cement-based composites. Cement Concr Compos 1992;14(2):105–18.
[35] Bažant ZP, Tabbara MR, Kazemi MT, Pijaudier-Cabot G. Random particle models for fracture of aggregate or fiber composites. J Eng Mech 1990;116 (8):1686–705.
[36] Mohamed AR, Hansen W. Micromechanical modeling of concrete response under static loading—part 1: model development and validation. ACI Mater J 1999;96(2):196–203.
[37] Yan P, Zhang J, Fang Q, Zhang Y, Fan J. 3D numerical modelling of solid particles with randomness in shape considering convexity and concavity. Powder Technol 2016;301:131–40.
[38] Xu W, Chen H. Numerical investigation of effect of particle shape and particle size distribution on fresh cement paste microstructure via random sequential packing of dodecahedral cement particles. Comput Struc 2013;114:35–45.
[39] Wittmann FH, Roelfstra PE, Sadouki H. Simulation and analysis of composite structures. Mater Sci Eng 1985;68(2):239–48.
[40] Wang ZM, Kwan AKH, Chan HC. Mesoscopic study of concrete I: generation of random aggregate structure and finite element mesh. Comput Struc 1999;70 (5):533–44.
[41] Häfner S, Eckardt S, Luther T, Könke C. Mesoscale modelling of concrete: geometry and numerics. Comput Struc 2006;84(7):450–61.
[42] Wriggers P, Moftah SO. Mesoscale models for concrete: homogenisation and damage behaviour. Finite Elem Anal Des 2006;42(7):623–36.

[43] Ma H, Song L, Xu W. A novel numerical scheme for random parameterized convex aggregate models with a high-volume fraction of aggregates in concrete-like granular materials. Comput Struc 2018;209:57–64.
[44] Fang Q, Zhang J. 3D numerical modeling of projectile penetration into rock-rubble overlays accounting for random distribution of rock-rubble. Int J Impact Eng 2014;63:118–28.
[45] Chen G, Hao Y, Hao H. 3D meso-scale modelling of concrete material in spall tests. Mater Struct 2015;48(6):1887–99.
[46] Xu Z, Hao H, Li H. Mesoscale modelling of dynamic tensile behaviour of fibre reinforced concrete with spiral fibres. Cement Concr Res 2012;42 (11):1475–93.
[47] Guo R, Ren H, Zhang L, Long Z, Jiang X, Wu X, et al. Direct dynamic tensile study of concrete materials based on mesoscale model. Int J Impact Eng 2020;143:103598.
[48] Malvar LJ, Crawford JE, Wesevich JW, Simons D. A new concrete material model for DYNA3D—release II: shear dilation and directional rate enhancements. Report. Glendale: Karagozian and Case Structural Engineers; 1996. Report No.: TM-96-2.1.
[49] Malvar LJ, Crawford JE, Morrill KB. K&C concrete material model—release III: Automated generation of material model input. Report. Glendale: Karagozian and Case Structural Engineers; 2000. Report No.: TR-99-24-B1.
[50] Jin Y, Chen T, Meng Q, Hu M. Difference of coral skeletal structure revealed by compressive strength measurements. J Trop Oceanogr 2017;36(2):33–9.
[51] Wang X, Wang R, Meng Q, Chen J. Research on characteristics of coral reef calcareous rock in Nansha Islands. Chin J Rocks Mech Eng 2008;27: 2221–6.
[52] Kim SM, Abu Al-Rub RK. Meso-scale computational modeling of the plastic-damage response of cementitious composites. Cement Concr Res 2011;41 (3):339–58.
[53] Wu Z, Yu H, Ma H. Study on the mechanical properties of new coral aggregate seawater concrete. Ocean Eng 2018;36(3):59–68.
[54] Yuan Y. Mix design and property of coral aggregate concrete [dissertation]. Nanjing: Nanjing University of Aeronautics and Astronautics; 2015.
[55] Zhou Z, Zou Y, Li X, Jiang Y. Stress evolution and failure process of Brazilian disc under impact. J Cent South Univ 2013;20(1):172–7.
[56] Neville AM. Properties of concrete. London: Pitman Press; 1981.
[57] Kadleček V, Modrý S, Kadleček V. Size effect of test specimens on tensile splitting strength of concrete: general relation. Mater Struct 2002;35 (1):28–34.
[58] Malhotra VM. Effect of specimen size on tensile strength of concrete. Appl Clin Inform J 1970;67(6):467–9.
[59] Neville AM. General relation for strengths of concrete specimens of different shapes and sizes. Appl Clin Inform J 1966;63(10):1095–109.
[60] Olesen JF, Ostergaard L, Stang H. Nonlinear fracture mechanics and plasticity of the split cylinder test. Mater Struct 2006;2006(39):421–32.